# Neuromechanical Phase Lags and Gait Adaptation in the Nematode *C. elegans*

Christopher J. Pierce,[1,2] Yang Ding,[3] Lucinda Peng,[2] Xuefei Lu,[2] Baxi Chong,[1] Hang Lu,[2] and Daniel I. Goldman[1]
[1]*School of Physics, Georgia Institute of Technology, Atlanta, Georgia 30332, USA*
[2]*School of Chemical and Biomolecular Engineering, Georgia Institute of Technology, Atlanta, Georgia 30332, USA*
[3]*Beijing University of Posts and Telecommunications, Beijing 102206, China*

(Received 1 May 2024; accepted 26 February 2025; published 3 April 2025)

Undulation is a form of propulsion in which waves of bending propagate along an elongated, slender body. This locomotor strategy is used by organisms that span orders of magnitude in size and represent diverse habitats and species. Despite this diversity, common neuromechanical phenomena have been observed across biologically disparate undulators, as a result of common mechanics. For example, neuromechanical phase lags (NPL), a phenomenon where waves of muscle contraction travel at different speeds than the corresponding body bends, have been observed in fish, lamprey, and lizards. Existing theoretical descriptions of this phenomenon implicate the role of physical body-environment interactions. However, systematic experimental variation of body-environment interactions and measurement of the corresponding phase lags have not been performed. Using the nematode *Caenorhabditis elegans* we measured phase lags across a range of environmental interaction regimes, performing calcium imaging in body wall muscles in fluids of varying viscosity and on agar. A mechanical model demonstrates that the measured phase lags are controlled by the relative strength of elastic torques within the body and resistive forces within the medium. We further show that the phase lags correspond with a difference in the wave number of the muscle activity and curvature patterns. Hence, the environmental forces that create NPL also act as a filter that shapes and modulates the gait articulated by the nervous system. Beyond nematodes, the simplicity of our model suggests that tuning body elasticity may serve as a general means of controlling the degree of mechanical wave modulation in other undulators.

DOI: 10.1103/PRXLife.3.023001

## I. INTRODUCTION

Understanding how organisms coordinate their bodies for effective locomotion is challenging. Locomotion emerges from the dynamics of interacting hierarchical systems that span length scales from cells to tissues and neural networks to whole bodies and beyond: locomotion also necessarily involves nontrivial interactions between the body and the immediate physical surroundings. Body-environment interactions are especially significant in organisms that rely on continuous body-environment contact for propulsion, such as snakes, fish, spermatozoa, and other lateral undulators. These organisms move by propagating bends along their elongated, slender bodies. They can be found in both wet and dry environments, span orders of magnitude in size, and operate in both dissipative (low Reynolds number (Re) fluid [1] or granular material [2]) and inertial (high-Re fluid [3]) regimes. Despite the diversity among undulating organisms, many share common, emergently simple neuromechanical dynamics.

For example, one common feature of undulation is the presence of so-called neuromechanical phase lags (NPL) [4–6]. To propagate a bend along the body, a wave of muscle activation $M(s,t)$ (where $s$ is the body coordinate and $t$ is time) is initiated and passed from head to tail. This wave of muscle activation and the resultant wave of body curvature $\kappa(s,t)$ generally do not travel at the same speed, producing a phase lag between $M$ and $\kappa$ whose magnitude varies along the body. Hence, maximal muscle activation and maximal curvature do not occur at the same point along the body.

NPL were first experimentally observed in inertial aquatic swimmers, such as bass [7] and eels [4]. To explain the origin of the effect, detailed, high-dimensional models incorporating large numbers of system-specific parameters (such as body taper and muscle nonlinearity) [5] were developed. Subsequently, the effect was observed in low-inertia situations, such as the swimming of sandfish lizards in sand [2,6], a frictional fluid. In this highly damped context, the analytical tractability of the drag forces revealed that NPL arise simply as a consequence of torque balance, and are therefore a generic feature of undulation mediated by body-environment mechanics [6].

Despite the implication that the phase lags depend on the particular form of body-environment interactions, existing models have only been tested using single organisms moving through a single environment; no systematic experimental variation of the body-environment interactions, and subsequent determination of the effect on the phase lags has been conducted. This is due, in part, to the experimental limitations of electromyography (EMG) recordings previously used to measure NPL in freely moving organisms [2,7], which provide limited spatial resolution. Furthermore, the limited range of environments in which typical vertebrate undulators locomote makes the systematic variation of body-environment

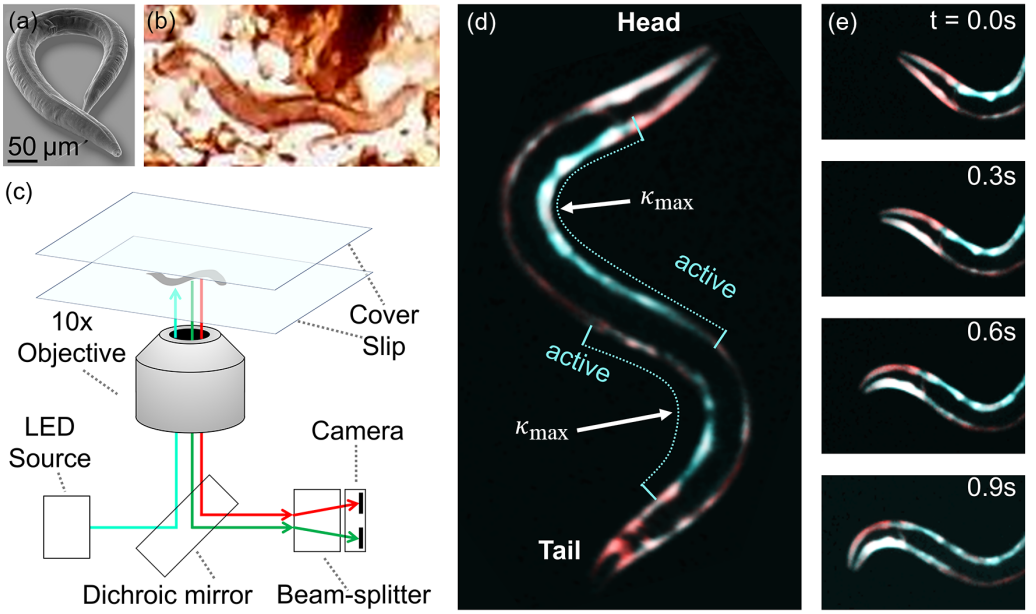


FIG. 1. *C. elegans* and muscle calcium imaging during locomotion. (a) A scanning electron microscopy image of *C. elegans* (courtesy of Ralf Sommer). (b) A worm crawling through a thin slice of a rotten peach, containing diverse rheologies. (c) Schematic of an imaging system for ratiometric calcium imaging. Worms swimming between two coverslips (or crawling on agar on a single coverslip) were illuminated in epifluorescence mode with a multi-color LED source. The output green and red channels were split with a beam splitter and sent to two halves of a single camera sensor. (d) False color image showing the calcium-sensitive GCaMP3 fluorescence signal (cyan) along with the calcium-insensitive RFP reference (red). Annotations indicate approximate regions of muscle activation and points of maximal curvature ($\kappa_{max}$). (e) Time series showing increasing calcium signal on the active body wall muscles as a head bend is initiated.

interactions challenging. Overcoming these constraints will help to quantitatively connect body material properties and environmental rheologies to the observed phase lags, thereby explaining the ultimate neuromechanical origins of the phenomena.

We overcome these challenges by employing the nematode *Caenorhabditis elegans* [Fig. 1(a)], an invertebrate undulator and widely studied model organism, which provides optical access to muscle activity through calcium imaging instead of invasive EMG probes. In the wild, *C. elegans* encounter complex heterogeneous terrain, such as the interior of rotting vegetative matter [Fig. 1(b)] [8]. In the laboratory, they can locomote in a wide range of synthetic environments (fluids with viscosities spanning orders of magnitude [9,10], viscoelastic fluids [11], granular media [12], and other heterogeneous terrains [13–15]). This combination of optical access to muscle activity and locomotory robustness permits systematic variation of the body-environment interactions while measuring phase lags. Hence, *C. elegans* is a valuable model for understanding how NPL is controlled by the environment, in general.

In this work, we measured body wall muscle activity [See Figs. 1(c)–1(e)] and body curvature simultaneously for worms undulating in fluids spanning several orders of magnitude in viscosity, and on agarose pads. This allowed the calculation of phase lags across a broad range of body-environment interaction regimes. We compare our results to a mathematical model based on the balance of external and internal torques and find good agreement, confirming that the magnitude and spatial variation of the neuromechanical phase lags are ultimately controlled by the relative importance of passive torques arising from within the body, and torques from the external environment, as suggested in Ref. [6].

## II. RESULTS

### A. Neuromechanical phase lags in *C. elegans* increase with viscosity

As noted above, points of maximum curvature and points of maximum muscle activation do not necessarily coincide. Furthermore, the amount of delay varies along the body, typically in the form of phase lag accumulation along the posterior region of the body. This effect is predicted to generally depend on the relative strength of torques from external resistive forces, such as viscous drag, and internal body forces, which are primarily determined by the passive material properties of the body [6]. The torque from the external drag at any point along the body is a sum of torques resulting from nearby and distant forces [6]. For example, the point forces $F_1$ and $F_2$ due to fluid drag illustrated in Fig. 2, contribute torques of opposite sign to the point $s_0$. In general, the viscous torque at any point $s$ is a nontrivial integral of the forces along the finite body, which produces a spatially varying torque profile whose maxima do not coincide with points of maximal curvature. In contrast, the body elastic torque is proportional to the local curvature and therefore maximal elastic torques coincide with points of maximal curvature [6]. Hence, the relative strength of internal torques and torques derived from external drag forces, as well as the nature of the external drag (i.e., frictional, viscous, etc.), determine the degree to which the active muscle torque needed to balance these passive forces is aligned or misaligned with the curvature.

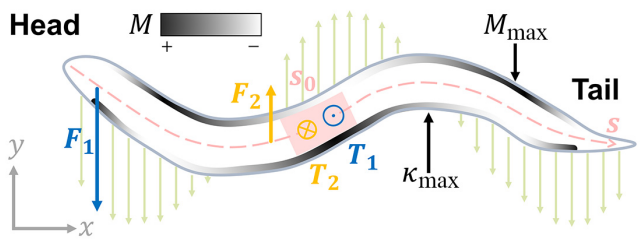


FIG. 2. Diagram of the theoretical model of an undulating *C. elegans*. Regions of muscle activity $M$ are schematically illustrated in each body wall muscle as a color gradient. Light green arrows indicate the approximate environmental resistive forces on the body during undulation. The net torque from environmental forces on a point $s_0$ is a sum of torques from all elements along the body. Examples shown are the torque $T_1$ (pointing out of the page) resulting from the distant point force $F_1$ and the torque $T_2$ (pointing into the page) resulting from the nearby point force $F_1$.

This mechanical model was initially derived for a generic undulatory swimmer and applied to the sandfish lizard *Scincus scincus* [6]. However, previous nematode-specific neuromechanical models also predicted phase lags to arise for worms crawling on agar pads, where drag forces dominate internal elasticity, but not in buffer swimming, where body elasticity is a larger contributor to torque balance [11,16]. To test these models, we measured muscle activity patterns via ratiometric calcium imaging in the body wall muscles [17,18] in *C. elegans* in a range of viscous fluids (buffer and 1–3 % methylcellulose (MC)) and on agar surfaces. This allowed us to experimentally determine the effect of different internal/external torque ratios on the phase lags.

To optically measure calcium activity in muscles, calcium-sensitive fluorophores, such as the family of GCaMP proteins [19], are expressed in particular target cells or tissues. Their fluorescence intensity increases with the local calcium concentration, and therefore when expressed in muscles indicates the degree of muscle activation [17]. However, because muscles necessarily contract and relax during movement, large changes in recorded intensity can also arise as the shape and projected area of the muscle cells change. Furthermore, motion artifacts and segmentation errors can lead to additional erroneous signals [20]. To mitigate these effects, typically a ratiometric approach [17,19,21] is used. A calcium-insensitive red fluorophore (RFP) is expressed in the body wall muscles along with a green calcium-sensitive GCaMP3, shown in Figs. 1(d), 1(e) and supplemental videos [22] (also see Sec. IV and Ref. [17]). By referencing the red, we can eliminate intensity variations that arise due to cell volume changes and movement. The measured ratio can therefore serve as a proxy for muscle activity, up to a constant time delay resulting from the protein kinetics [17,19,21].

To determine the phase lags, we first calculated the GCaMP-RFP signal ratio within the body wall muscles see Figs. 1(d) and 1(e) at each point along the body, along with the corresponding body curvature at each point, for all environments. We note that because these experiments were conducted with early L3 stage animals (24 h post-hatch), identification of the dorsal and ventral sides was not possible. We, therefore, refer to the two body-wall muscles relative to the direction of motion, referring to the $y_+$ side for muscles to the left of the direction of motion ($x$) and the $y_-$ side for muscles to the right (see the coordinate system in Fig. 2). Figures 3(a) and 3(b) show the ratiometric calcium signal for the $y_+$ and $y_-$ body wall muscles, respectively, and the curvature oscillation at the midpoint along the body for an example collected from buffer [Fig. 3(a)] and crawling on agar [Fig. 3(b)]. The activity patterns of the two body wall muscles are approximately 180° out of phase as expected based on their contralaterally inhibited connectivity [23] but have an overall phase shift relative to the curvature oscillations.

By computing analogous curves for a set of points extending from head to tail, we can construct space-time plots of muscle activation that can be compared with the corresponding curvature patterns, shown in Figs. 3(c)–3(f). These results reveal differences in the overall shape of muscle and curvature waves in both buffer and agar, evident in the variations in the wave speed of each respective quantity along the body. This can be visualized by comparing the slope of the line of zero crossings in muscle waves and curvature waves [blue and green curves in Figs. 3(e) and 3(f)].

Neuromechanical phase lags were calculated from the spatiotemporal muscle/curvature data using a cross-correlation technique, which helped mitigate the effect of noise in the muscle signal (see Sec. IV). As noted above, the protein kinetics produce an overall delay of the GCaMP signal relative to muscle activation, which we have not taken into account. Hence, the absolute magnitude of the phase lags is ambiguous. However, as previously shown in Ref. [17], the delay in protein kinetics is independent of the environment, hence the relative phase lags of different parts of the body may be determined, without taking the overall delay into account.

In buffer and in 1% MC solutions, phase lags were approximately constant along the body (Fig. 4). A small decrease in the mean phase lag along the midbody can be observed in buffer, however, these shifts were statistically insignificant. A two-sample $t$ test indicated no statistically significant difference between the phase lag distribution at the head with any of the other segments along the body. Similarly, the marginal increase in the mean phase lag along the body in 1% was found to be statistically insignificant.

As the wt% was increased, and also on agar surfaces (thought to have higher overall resistive forces than the viscous fluids considered here [11]), phase lags began to accumulate significantly along the midsection of the body, with phase lag distributions in posterior regions that were statistically distinct from the distribution at the head. Across these environments, we also observed a small decrease in the relative phase lag near the head and in the most posterior region of the worm, we also observed a decrease in phase lag. Overall, we observe a local phase advance in the regions near the head and tail, and a consistent, viscosity-dependent phase lag accumulation along the middle of the body, similar to previous observations of NPL [5,6].

Taken together, our results suggest that in lower viscosity environments the relative phase lag across the body is approximately constant. As the resistance in the environment is increased (by either increasing viscosity or by switching to a solid gel surface), asymmetric phase lag

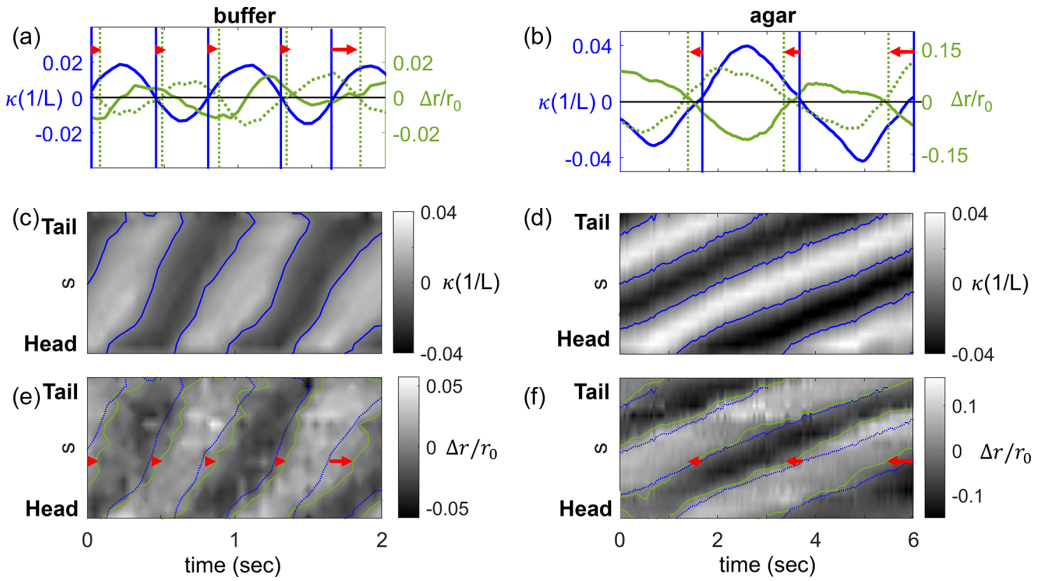


FIG. 3. Body curvature and muscle activation patterns in buffer and agar. (a) Ratiometric calcium signal from body wall muscles on the $y_+$ and $y_-$ sides of the body over time (solid and dotted green curves, respectively), along with body curvature oscillations (blue curve, in units of $1/L$ where $L$ is the body length). These data were collected at a point near the body midpoint for an individual worm swimming in buffer. The same quantities are shown in (b) but for an individual worm crawling on agar. Red arrows indicate a phase shift between zero crossings (marked by vertical lines) in curvature and muscle activity oscillations. (c), (d) Heatmaps show the curvature variation along the body coordinate $s$ (vertical axis) and through time (horizontal axis) in buffer (c) and agar (d), with points of zero curvature highlighted in blue. (e), (f) Corresponding muscle activity heat maps with zero crossings highlighted in green and with curvature zero crossings overlaid (blue). These heat maps also correspond with the curves in (a) and (b). Red arrows indicate the difference in the zero crossings of curvature and muscle waves indicating accumulating phase lag in the posterior region for agar (f).

accumulation along the posterior region increases in magnitude, in accord with prior qualitative predictions based on torque balance [6]. These results also display good agreement with a previous neuromechanical model of *C. elegans* from Denham *et al.* [16] and an earlier biomechanical model from Shen *et al.* [11]. These models predict an approximately flat neuromechanical phase lag profile across the body for swimming in buffer, but for agar crawling predicts phase accumulation along the body.

Notably, most vertebrate systems appear to operate in phase lag regimes similar to those observed for worms in high-resistance environments, displaying anterior-posterior phase lag accumulation. This suggests that they all operate in regimes where the external drag forces are the most significant determinant of the phase lags (relative to internal forces). Our results suggest that across environments, *C. elegans* interpolates smoothly between the different regimes predicted in Ref. [6]. Agar and high-viscosity environments reproduce the spatial phase lag profiles of both dry, inertial sand-swimming

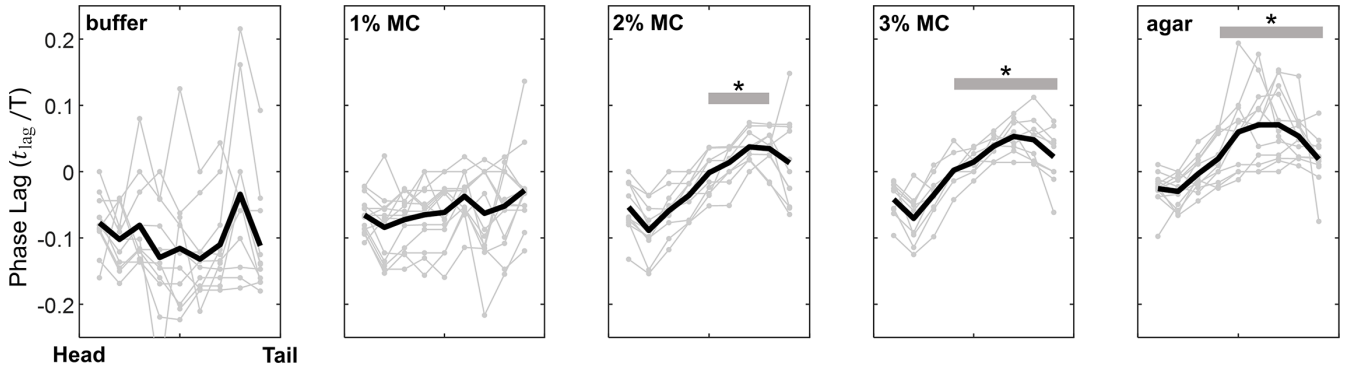


FIG. 4. Phase difference between muscle and curvature waves for different points along the body and different environments. Curves for individual animals are shown in gray and the population average is shown in black for buffer ($N = 12$), 1% MC ($N = 14$), 2% MC ($N = 11$), 3% MC ($N = 10$), and agar ($N = 12$). At lower viscosities (buffer, 1% MC) the phase lags are approximately constant along the body. As the viscosity increases or in agar, a phase lag develops along the body before decaying downward in the most posterior regions. A two-sample $t$ test was used to make pairwise comparisons between the phase lag distribution at the head and the phase lag distribution at each posterior point along the body. Gray bars indicate the set of points along the body where phase lag distributions were statistically different from the head ($p < 0.03$, two-sample $t$ test).

vertebrates [6] and wet, high-Re aquatic swimmers [5]. In contrast, lower viscosity regimes resemble the theoretical prediction for a body elasticity-dominated torque balance [6], previously not seen in experiment.

Having described the effect of the environmental forces on the phase lags, we now proceed to examine differences in muscle and curvature wave shapes and speeds in detail, and to discuss the implications of this phenomena for environmentally adaptive gait control.

### B. Environmental interactions shape undulatory waves and shorten wavelengths

As noted above, phase lags can only occur if there is a difference between the phase velocity of the muscle wave $v_m$ and the curvature wave $v_{\text{curv}}$. This requires that either the frequency $f = 1/T$ or wave number $k = 1/\lambda$ of the two respective waves must differ, which in turn implies that the gait created by the neuromuscular system (the muscle activity pattern) necessarily differs from the gait executed by the body, due to passive mechanical effects.

Across all body segments and environments, the frequencies of the curvature and the muscle waves, as determined from fits to sine functions, are matched [Fig. 5(a)]. Hence, differences in phase velocity across the body arise from changes in the wave number. To determine the wave number difference, we calculated the wave number shift implied by a given phase lag profile using measured phase lags as an input.

The phase difference $\phi$ between two sinusoidal traveling waves with wave numbers $k_m$ and $k_{\text{curv}}$ and a common frequency $f$ is given by

$$\phi = \phi_m - \phi_{\text{curv}} \tag{1}$$

$$= 2\pi(k_m s - ft) - 2\pi(k_{\text{curv}} s - ft) \tag{2}$$

$$= 2\pi(k_m - k_{\text{curv}})s. \tag{3}$$

We can therefore relate the change in measured time lags $t_{\text{lag}}$ across a distance $\Delta s$ along the body to the resultant wave number difference via

$$\frac{\Delta t_{\text{lag}}}{T\,\Delta s} = \frac{\Delta\phi}{2\pi\,\Delta s} = k_m - k_{\text{curv}}. \tag{4}$$

Because the phase lags do not simply increase linearly along the body, we estimated the approximate effective wave number shift using the average difference in phase across a region in the middle of the body, avoiding the most anterior and posterior body segments (this helped to mitigate deviations from linearity near the head and tail). The resulting wave number shifts are shown in Fig. 5(b). As the viscosity is increased, an initial positive wave number shift in buffer (where $k_m > k_{\text{curv}}$) gives way to a larger negative wave number shift ($k_m < k_{\text{curv}}$) in the higher resistance environments.

Beyond wave number shifts, the nonuniformity of the phase lags along the body imply differences in the overall shape of muscle and curvature waves and different overall deviations from the sinusoidal idealization. While many approaches approximate both the body kinematics and muscle activity patterns as traveling sine waves [6], the measured waves display significant deviations from sinusoidal shapes.

To describe the average shape across time and populations, we computed population-averaged covariance matrices for both muscle and curvature waves using the same data set used to calculate the phase lag and kinematic data described above, shown in Fig. 6, left and center columns. The width of the central lobe along the diagonal is proportional to the wave speed [and therefore the effective wave numbers shown in

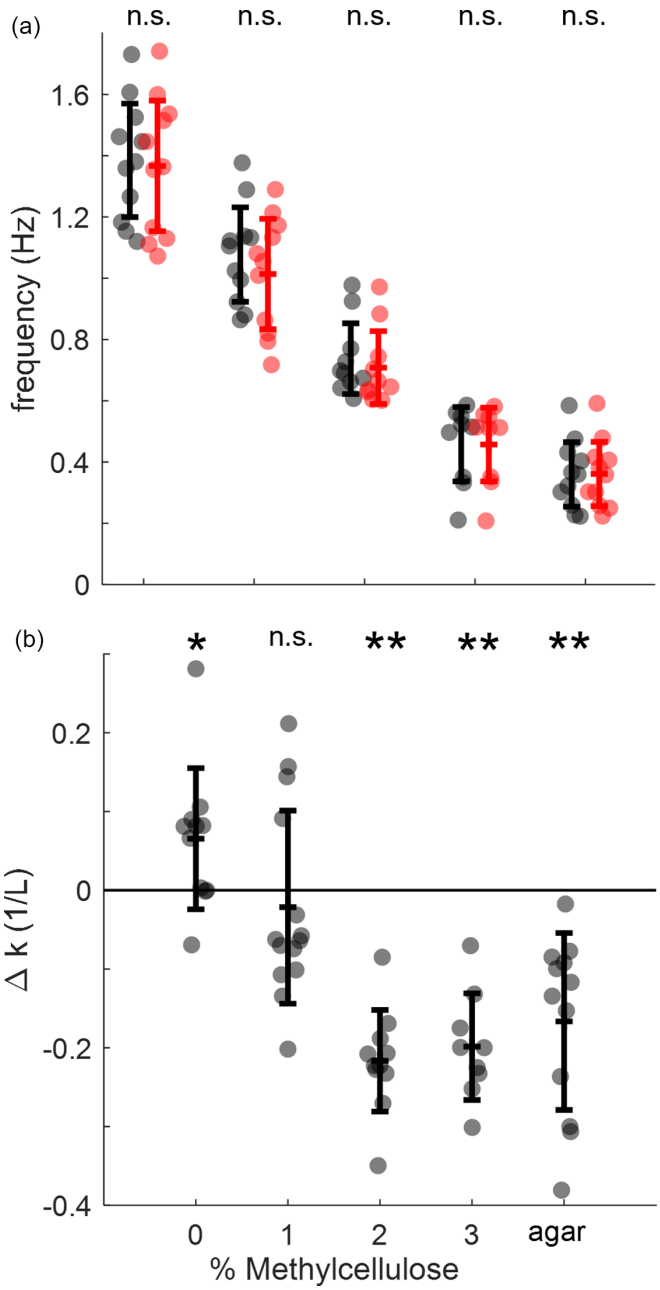


FIG. 5. Undulatory wave parameters across the different environments for the same animals used to measure phase lags (Fig. 3). (a) Muscle and curvature waves are frequency-locked for all environments. A two-sample $t$ test showed no significant differences between muscle and curvature frequencies for all environments. However, wave numbers shift (b). In stiffer environments (2–3% MC and agar) a negative shift in wave number is observed ($k_m < k_{\text{curv}}$), while in buffer a marginally significant positive wave number shift ($k_m > k_{\text{curv}}$) is observed. In 1% MC no significant wave number shift is observed. ** indicates $p$ value $< 0.03$, * indicates $p$ value $< 0.05$ from two-sample $t$ test.

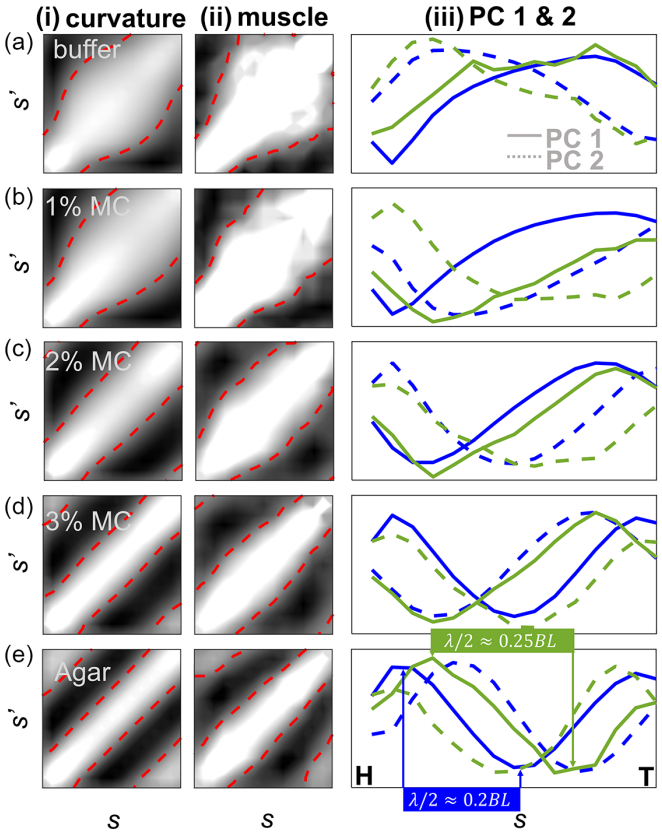


FIG. 6. Wave shape differences account for observed phase lags and wave number shifts. Population and time-averaged covariance matrices for curvature waves (i) muscle activity waves (ii) and corresponding PCs 1 and 2 (iii) for curvature (blue) and muscle activity (green). (a)–(e) show the same quantities for buffer, 1% MC, 2% MC, 3% MC, and agar, respectively. Covariance matrices and PCs were calculated using the same set of individuals used to calculate phase lags and wave number shifts. PCs also indicate a difference between the wavelength of muscle and curvature patterns, consistent with wave number shifts (Fig. 5).

Fig. 5(b)], and can hence be used to visualize the variation of the speed along the body.

In lower resistance environments, the variation of wave speed along the body in both the muscle and curvature waves increases to the midpoint, before tapering back to a slower speed in the posterior region of the worm. As the resistance of the medium is increased, the speed variation in the curvature wave is reduced relative to the corresponding muscle wave. [See for example the relative constancy of the node lines in the agar covariance matrices relative to the corresponding matrix for the muscles, Fig. 6(e).]

We can further visualize differences in wave shape (and wave number), by examining the first two principle components of each respective wave (the first two eigenvectors, or eigenworms [24] of the covariance matrices, right column, Fig. 6). Figure 6(e) highlights the peak-trough distance in the muscle waves, illustrating the wave number difference discussed above reflected in the shapes of the PCs. Taken together, these results indicate external forces not only induce wavelength shifts. They also shape the wave created by the nervous system, rectifying wave speed variations along the

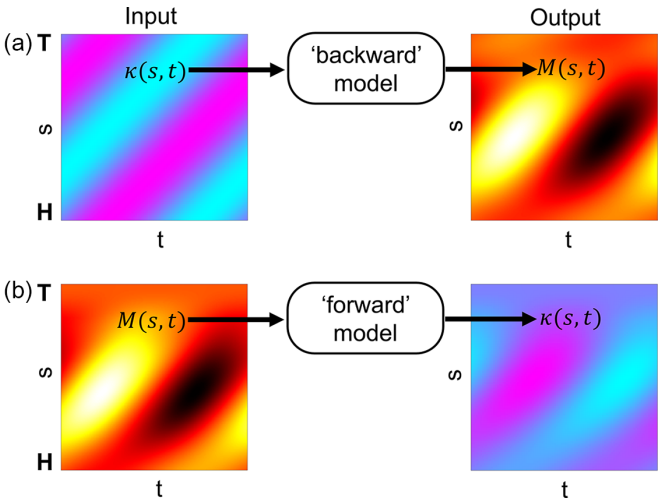


FIG. 7. Illustration of the two modeling approaches for estimating phase lags during swimming in different environments. The backwards model (similar to that in Ref. [6]) is shown schematically in (a). This model takes the kinematic gait parameters as an input and uses torque balance to solve for the muscle torque pattern needed to produce the input kinematics in a particular environment (e.g., at a particular viscosity). (b) A forward model takes a muscle torque pattern as an input and solves for the time-dependent body kinematics. (Note that H indicates head position, T indicates tail.)

body to produce a wave that more closely resembles a traveling sine wave.

### C. Relative strength of viscosity and body elasticity controls passive mechanical wave modulation

We have observed that phase lags accumulate along the body as environmental resistance increases, and self-consistently, that wave number and ultimately wave speed differences produce the observed phase lags. Previous models predicted that body elastic torques are in phase with body curvature [6] and hence produced negligible phase lag accumulation. In contrast, large external torques (e.g., viscous) were predicted to produce phase lag accumulation. We, therefore, hypothesized that our experimentally observed phase lag trends arise because internal elastic torques dominate in the less resistive environments, and that the observed phase lag accumulation in higher viscosities and agar arise from external drag dominance. To test this, we modified a previous resistive force theory (RFT) model, which incorporated torque balance [6,25], to systematically test the effect of different elastic/viscous torque ratios on the predicted phase lag.

We first constructed a model that takes observed curvature as an input and calculates the internal torque demand from the muscle [see schematic in Fig. 7(a)]. We assume the curvature has a traveling wave form $\kappa(s,t) = A_\kappa \sin(2\pi f t + 2\pi s/\lambda)$, where $\kappa$ is the curvature of the midline of the body, $s \in [0\ L]$ is the arc length along the midline, $A_\kappa$ is the amplitude, $f$ is the frequency, $t$ is time, and $\lambda$ is the wavelength. If the translational velocity and rotation speed of the body are known, then the velocity on each segment can be calculated. The forces on each infinitesimal segment are computed as proportional to their velocities in the normal and parallel directions, namely

$F_n = C_n v_n$ and $F_l = C_l v_l$. The drag coefficient in the normal direction is greater for slender bodies and anisotropy of the drag force is described by the ratio $\mathrm{DA} = C_n/C_l$. Given the negligible inertia, we employ force and torque balance equations, expressed as $0 = \vec{F}_{\mathrm{total}} = \int_0^L \vec{F}(s')\mathrm{d}s'$ and $0 = \vec{T}_{\mathrm{total}} = |\int_0^L \vec{F}(s') \times \vec{r}(s')\mathrm{d}s'|$, where $\vec{r}(s')$ denotes the position of a body segment at arc length $s'$ from the tail. These equations allow us to determine the swimmer's translational and rotational motion within the plane.

The required torque (bending moment) generated by the muscle is calculated as the sum of the torques required to overcome the external viscous drag and the elastic force of the body: $\vec{T}(s) = \vec{T}_e(s) + \int_0^s \vec{F} \times [\vec{r}(s') - \vec{r}_s]\mathrm{d}s'$ (see Sec. IV for details). From the torque by the muscle we infer the muscle activation and compute the phase lags by comparison with the input kinematics. Figure 8(a) shows that this backward kinematic model reproduces the experimentally measured phase lag profiles and captures the effect of increasing viscosity. This suggests that the relative magnitude of internal and external forces controls the onset of phase lag accumulation with viscosity. While previously measured phase lags were observed solely in organisms occupying the external-drag-dominated regime, *C. elegans* interpolates between the two regimes as it moves through increasingly viscous media.

In addition to the phase lags themselves, we also used our backward model to calculate the wave number of the muscle activation wave and find reasonable agreement to experimental values [see Fig. 8(c)]. This shows that in our model, as well as in experiments, the phase lags co-occur with wavelength shifts, implying that in cases where phase lags are large, there exists a significant discrepancy between the muscle wave number and the wave number of the gait that results.

Finally, we asked whether phase lags and their variation in different environments could, in principle, arise solely from mechanical interactions without sensory feedback. To do so, we ran our mechanical model forward [see Fig. 7(b)]. We started with a single muscle pattern, obtained from the backward model's prediction of the muscle torque when the wave number of the curvature wave is 1.5, and slightly adjusted the tail part to ensure a monotonic phase change over the body. Using this muscle torque as our input, we solved for the curvature as a function of time and position with the same constraints in the backward model, namely the force and torque balance, anisotropic force relations with velocity at each body segment, and elastic body torque proportional to curvature. Then we varied the strength of viscous forces, scaled the muscle pattern with a single factor according to the observed overall magnitude, and solved the forward problem to produce the corresponding kinematics.

We found that similar phase lag profiles may be obtained [see Fig. 8(b)], implying that simply tuning the viscosity, in the absence of active changes to the wave number of the muscle pattern can in principle produce phase lags and the corresponding wave number modulation entirely through passive mechanics. While *C. elegans* does not appear to make use of a purely passive strategy, these results suggest that viscous-dependent phase lags and wave number modulation are a generic feature of undulation that do not require active wave number shifts to accompany changes in viscosity.

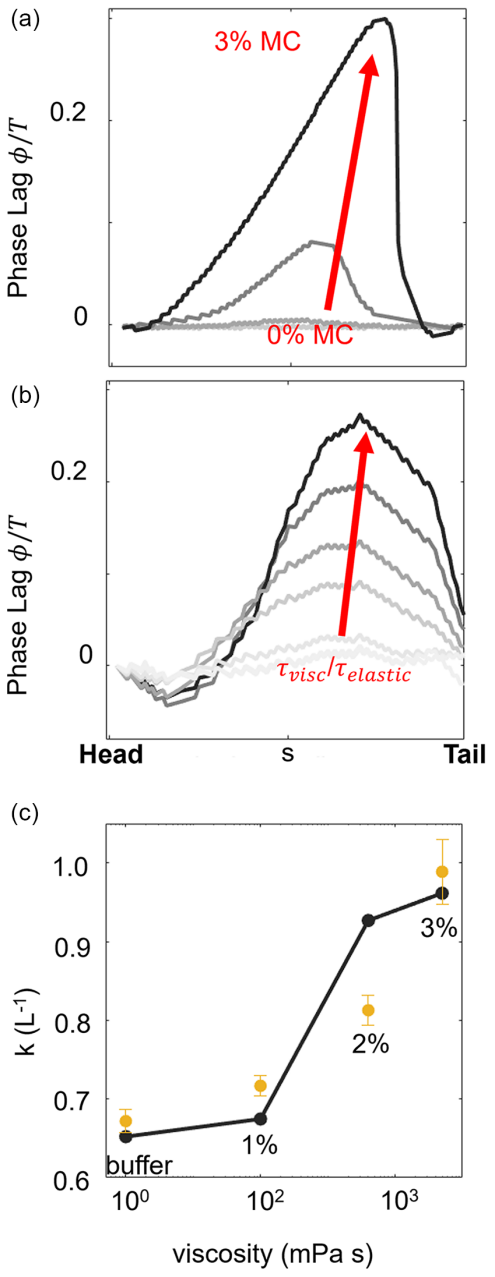


FIG. 8. Model predictions for phase lags and wave numbers. The "backward" model displays qualitative agreement with experimental data, showing phase lag accumulation that increases with external viscosity (a). Panel (b) shows the results of the "forward" model for an input muscle torque pattern based on muscle patterns of a worm swimming in buffer. The viscosity of the environment was then tuned without changing the underlying muscle pattern. This demonstrates that phase lag accumulation can arise purely passively as viscosity is increased without concurrently changing the underlying muscle wave. (c) The 'backward' model also predicts the approximate muscle activation wave numbers. Yellow points show the experimentally measured wave number, where error bars indicate the standard error of the mean across the population. Black points indicate the calculated muscle wave number from the backward model.

## III. DISCUSSION AND CONCLUSION

Fundamentally, phase lags arise because, for any slender undulator, the muscle acting at a point $s$ must balance not only torques originating from nearby body segments but also from distant points along the body—simply because the torque acting at a point $s$ is a sum of torques from point forces acting at all points between $s$ and the end of the body [6]. In this way, the neuromechanics of undulation differs from certain limbed systems with small numbers of joints: the muscle acting on a particular joint may be insensitive to the activity of faraway joints and other limbs. For undulators, the muscle acting at a point $s$ balances a sum of torques that arise both from fundamentally different forces (e.g., external fluid drag, the internal forces from body viscoelasticity), but also acting at points along the entire body.

These different torque contributions can be either in phase (their maxima coincide with the max curvature) or out of phase with the bending wave (their maxima are misaligned with peak curvature). Hence, their relative strength determines whether and to what degree muscle activity coincides with the curvature profile along the body. Specifically, a previous analytical calculation has shown that external drag (e.g., granular or viscous) produces torques that are typically out of phase with curvature while the internal torques arising from body elasticity, for example, are in phase [6]. Hence, the relative strength of internal and external passive torques, as set by the mechanical properties of tissues and the surrounding environment determine the size and spatial variation in the phase lags.

We have illustrated this effect experimentally using nematodes, finding that as environmental drag is increased relative to body elasticity, neuromechanical phase lags begin to accumulate along the body. This observation is consistent with the predictions of neuromechanical models of nematodes crawling on agar [11,16] and also with a simple, mechanical model developed to describe vertebrate undulation [6,25].

In contrast to measurements of NPL via EMG recordings, the spatial resolution afforded by an optical approach has enabled us to compare the wave shapes of muscle and curvature waves. Pierce-Shimamora *et al.* [26] compared muscle activity patterns in buffer and agar and found substantial differences; however, their reported muscle patterns did not appear to take the form of a smoothly traveling wave of activity, making determinations of phase lags and the wavelengths of muscle activity patterns prohibitively difficult. Butler *et al.* [17] measured muscle activity patterns in a broad range of viscosities and on agar, and found that the average phase lag across the entire body remained consistent across environments, but did not report the spatial profile of the phase lags across environments. Both of these studies employed young adult worms, which we found produced inconsistent optical signals, possibly due to the variable extent of agar depression resulting from movement, the size (diameter) of the animals, the presence of vulva muscles and inconsistencies of myosin expression after development. In this work, by instead employing larval worms at the L3 stage, we found consistent wavelike activity. The general trends we observe in larvae are likely to generalize to adult worms. The body elasticity of *C. elegans* is known to increase as the body diameter increases across development [27]. Similarly, increases in body diameter should increase the size of viscous body torques. Thus, increasing environmental viscosity should also lead to an increase in the phase lags for adult worms. However, the magnitude of the effect may differ from L3 stage larvae, depending on the scaling of the elastic and viscous terms.

These results showed that phase lags arise due to differences in wave speed variation along the body and corresponding shifts in the wave number between neuronally generated muscle activity patterns, and the curvature waves that result. We, therefore, concluded that environment-dependent wavelength tuning in *C. elegans* is not solely controlled by neural feedback but through a combination of neural and passive mechanical effects. The passive mechanical wave number shifts are controlled by the elasticity of the body relative to the environmental drag.

For other undulators, including previously studied vertebrate systems, this means the NPL also produces a wave number discrepancy between muscle and body curvature waves, and in general, torque balance in the majority of environments requires modulation of the wave pattern created by the nervous system. This is important in highly dissipative, noninertial environments, such as low-Re fluids, agar gels, or the movement of a sandfish in sand (a frictional fluid), because the lack of inertia means that performance metrics depend solely on geometry. In low-inertia situations, the wavelength and amplitude fully determine the performance of a particular gait (for example, the displacement per undulation cycle). Thus, wave number selection is an important determinant of performance.

Moreover, resistive force theory calculations show that the displacement per undulation cycle is a non-trivial function of the wave number, leading to optimally performing wavelengths that change with environmental parameters, such as drag anisotropy. This explains, in part, why *C. elegans* selects higher wave numbers as environmental resistance increases. While viscous fluids typically produce a drag anisotropy of $\sim$1.5 [28], higher resistance environments, such as agar surfaces, have produced higher measured drag anisotropies, estimated to be as high as $\approx$110 [11,29]. Figure 9 shows the relationship between predicted displacement per undulation cycle and wave number for a worm under viscous drag anisotropy (and using the measured body bending amplitude $\kappa L$) in buffer and for estimated agar drag anisotropy (and using the measured body amplitude observed during agar crawling). As the drag anisotropy is increased, the most kinematically efficient wave numbers are larger, corresponding with greater efficiency at shorter wavelengths. Because the effect of mechanics in more resistive environments is to shift wave numbers upward relative to the muscle wave number, these passive mechanical effects enhance this process, meaning that achieving a better wavelength with passive effects would reduce the requirement of larger control changes from the nervous system.

Beyond comparisons of buffer and agar, similar arguments may apply to the methylcellulose experiments. While an ideal Newtonian fluid should have a drag anisotropy of $\sim$1.5 [28] for all viscosities, MC solutions increase viscosity through the addition of long, polymer molecules, which are likely to increase drag anisotropy relative to the ideal Newtonian case. In general, if drag forces are accompanied by an increase in

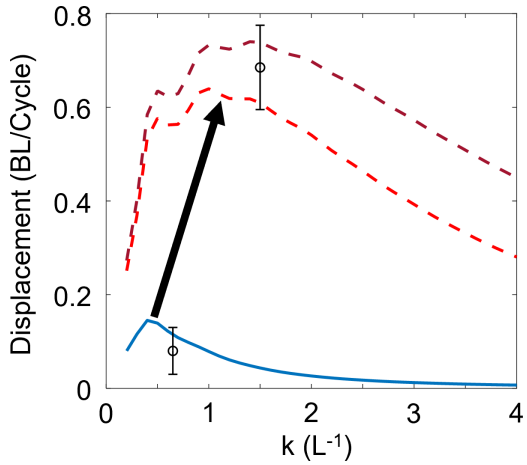


FIG. 9. RFT prediction for the displacement per undulation cycle (in units of body length per cycle) for agar surfaces (dashed lines) and buffer (blue lines) vs. wave number along with experimentally observed displacement vs wave number for buffer and agar. Error bars indicate the standard error of the mean of the population. The RFT calculation used previous estimates of the drag anisotropy for buffer (DA = 1.5), and agar (DA = 10, 20) as well as measured dimensionless curvature amplitudes ($\kappa L = 1.5$ for buffer and $\kappa L = 7.7$ for agar).

drag anisotropy, as is likely the case in many non-Newtonian biological fluids, the passive mechanical wave modulation leads to higher locomotion performance.

Figure 10 summarizes our model of the role of mechanics in nematode gait adaptation. As the strength of viscous environmental drag is increased, passive mechanics as well as mechanosensory neural feedback work together to select an environmentally adaptive gait. Future descriptions of nematode locomotion control should consider effects outside the nervous system. Beyond nematodes, NPL likely causes changes between muscle patterns and actual gait wave parameters. While most previously measured examples of NPL appear to be in the high drag regime of nematodes (with negligible body elasticity relative to the muscle torque), other organisms where body elastic torques and environmental torques are comparable may display similar shifts in NPL spatial patterns upon environmental changes. These results may also suggest a new paradigm for gait selection in undulatory robots if the mechanics of robot-environment interactions [15] could be appropriately tuned to leverage the mechanical control scheme employed by nematodes, but generalized to other, complex terradynamic terrains.

## IV. METHODS

### A. Strains

Strains were maintained at 20 °C and were fed *E. coli* (OP-50) bacteria on agar plates using standard protocols [30]. The transgenic lines AQ2953 ljIs131[Pmyo-3::GCaMP3-SL2-tagRFP-T] and AQ2954 ljIs132 [Pmyo-3::GFP-SL2-tagRFP-T] [17] were used to perform calcium imaging

### B. Calcium imaging

Calcium imaging experiments were performed on a standard wide-field epifluorescence microscope described previously in Ref. [31]. Synchronized worms in stage L3 (see Sec. II above for discussion of the use of stage L3) were

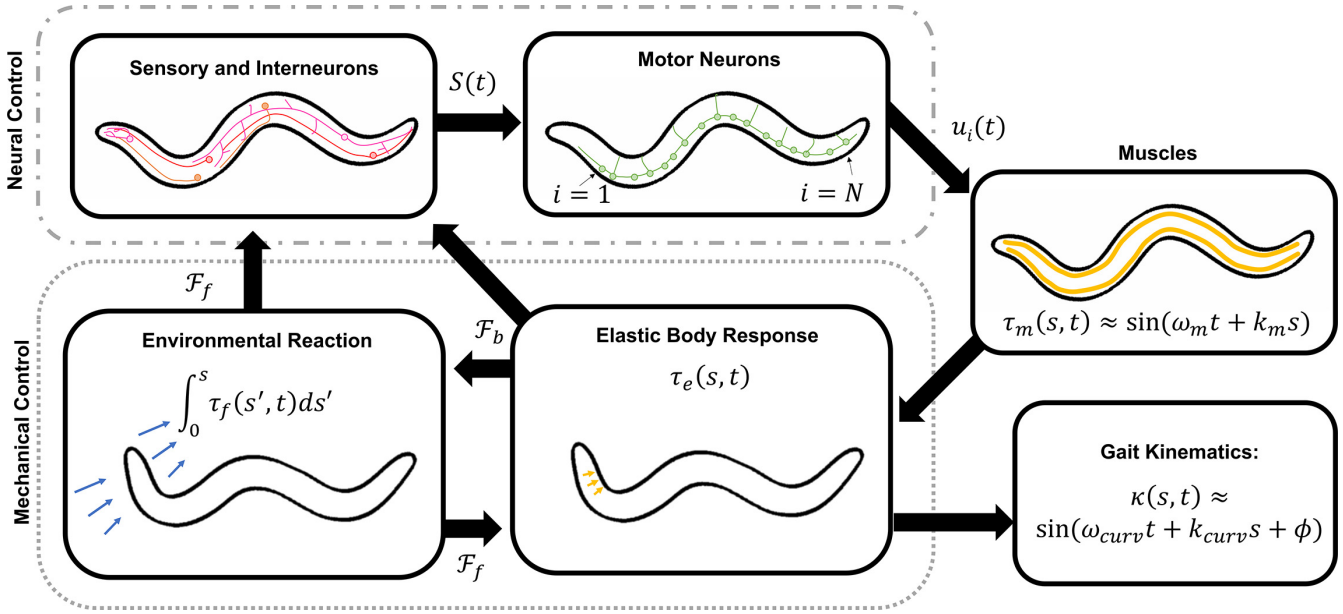


FIG. 10. Neuromechanical system diagram for nematode gait adaptation. Mechanosensory neurons sense external and internal physical forces, which depend on the resistance of the environment. These mechanosensory neurons pass signals to the interneurons which integrate and process the signal before sending commands S(t) to the motor neurons. The $N$ motor neuron groups distributed along the body pass signals $u_i(t)$ to contract/relax downstream muscles, which respond by creating a torque wave $\tau_m(s,t)$. The torque wave is then functionally modulated by the elastic body forces and external environmental torques to produce the final gait kinematics $\kappa(s,t)$. Both mechanical and neural control interact to perform environmentally dependent gait adaptation.

placed either on an agarose pad or into a small droplet of fluid between two coverslips separated by a kapton tape spacer. The fluids used were S-basal buffer solutions with varying weight percentages of methylcellulose (from 0–3%) to provide a range of viscosities.

### C. Image processing

Videos were manually cropped to sections containing bouts of forward locomotion without transients or reorientation behaviors and analyzed using protocols similar to Refs. [18,32]. RFP and GCaMP channels were aligned using MATLAB's IMREGISTER function. After registration, the red channel was used to segment the worm body using the canny edge detection algorithm to create a mask over the worm body in the coordinates of the registered images. This mask was then skeletonized to identify the centerline of the worm body. This centerline was subsequently smoothed using a B-spline function and used to calculate the curvature across the body as a function of time. The centerline was also used to define different muscle regions along the body in conjunction with the mask. A line normal to each point of the splined centerline was calculated and used to divide the worm into 100 discrete segments per side. Segments were made of quadrilaterals formed by intersecting the normal lines associated with two adjacent spline points with the edge of the mask. The intensity in each segment was calculated for each time point and then scaled by the number of pixels. Additionally, a small region with a fixed distance outside the worm mask was used to calculate local background intensity. The local background was subtracted from each segment in both the red and green channels, and finally, the ratio of green to red was computed.

In some cases, worms displayed consistent baseline shifts in the ratio along the body. To remove these shifts, the time average of the ratio was computed for each discrete body segment and subtracted off. Finally, to improve signal-to-noise in subsequent calculations, at the expense of spatial resolution, multiple adjacent segments were averaged creating larger blocks. For phase lag calculations segments were grouped into nine segment blocks spanning from head to tail, and for wave shape calculations requiring higher spatial resolution segments were grouped into 15 blocks.

### D. Phase lag calculation

To compute phase lags, the average temporal period of the curvature wave $\kappa(s_i, t)$ was first computed for each segment block by first calculating the time-time autocorrelation for a given block $i$, and averaging the distance between adjacent peaks. Then, the phase lags were computed by calculating the cross correlation of the muscle activity with the curvature, determining the shift of the central maximum from zero, and scaling by the temporal period of the curvature wave. To average over both body wall muscles, the left side relative to the direction of crawling was inverted before calculating the cross correlation. $m_l(s_i, t)$ to eliminate the contralateral phase shift of 180 degrees. This was performed for $N = 9$ segments moving from head to tail.

### E. Numerical model

We used two models to compute the relative phase between the curvature and the torque generated by the muscles. In both models, the body of the nematode was considered as a uniform cylinder with a length $L = 1.1$ mm. The overall motion of the nematode is computed using the classic resistive force theory (RFT) [33]. In RFT, the body of the nematode was divided into infinitesimal segments, and the forces $\vec{F}$ were decomposed into forces normal to the axis (midline) of the cylindrical body $F_n$ and the forces parallel to the axis $F_l$. The forces were proportional to the respective velocity components, i.e., $F_n = C_n v_n$ and $F_l = C_l v_l$. The drag coefficient in the normal direction was taken as $C_n = 3.3\eta$, where $\eta$ is the viscosity of the fluid. The motion of the nematode was constrained in a plane, and the three degrees of freedom were considered. Assuming the inertia is negligible, the force (torque) balance was reached at every moment. Then the translational and rotational velocities were obtained. Since the anisotropy is unknown and the swimming speed was measured, we tuned DA to match the swimming speed. Although the anisotropy has a significant effect on swimming speed, it affects the pattern of the torque little. The difference between the wavelengths of the torque generated by a constant anisotropy DA = 1.6 and speed-matched values is less than 5%.

In the backward model, the kinematics was prescribed as a traveling wave $\kappa(s, t) = A_\kappa \sin(2\pi f t + 2\pi s/\lambda)$, where $\kappa$ is the curvature of the midline of the body, $s$ is the arc length along the midline, $A_\kappa$ is the amplitude, $f$ is the frequency, $t$ is time, and $\lambda$ is the wavelength. These kinematic parameters were set as those values from the experiments. At every time point, the orientation of the body segment at $s$ in the body frame is computed using the curvature as $\theta_b(s) = \int_0^1 \kappa \mathrm{d}s$, and the positions of the segment is computed as $\vec{r}_s = [x(s), y(s)] = [\int_0^1 \cos(\theta_b)\mathrm{d}s, \int_0^1 \sin(\theta_b)\mathrm{d}s]$. The velocity of the segment can be computed as $\vec{v}(s) = \dot{\vec{r}}(s)$. With the unknown rotational speed $\omega_b$ and translation velocity of the tail $\vec{v}_{\text{tail}}$, the velocity at $s$ on the body can be computed as $\vec{v}_{\text{lab}} = \vec{v}_{\text{tail}} + \omega_b \vec{e}_z \times \vec{r} + \vec{v}(s)$. After the motion was solved, we computed the torque based on the force distribution along the body as $T(s) = T_e(s) + \int_0^s \vec{F} \times [\vec{r}(s') - \vec{r}_s]\mathrm{d}s'$. The torque contribution from the body elasticity was $T_e(s) = b\kappa(s)$. The elasticity of nematode body had been measured previously in several studies, but the values spanned a few orders of magnitude, and the values were obtained with anesthetized worms [10,27,34]. Nonetheless, it is safe to say that the torque from elasticity is significant when nematodes swim in low-viscosity environments. Therefore, we varied the body elasticity $b$ in the range of 2–200 $\times 10^{14}$ N m$^3$. The torque contribution from the body viscosity is negligible and hence not considered in our model, according to a previous study [10].

In the forward model, the muscle torque pattern was fixed and prescribed as a traveling wave pattern [see Fig. 7(b) for the constructed torque pattern]. This torque pattern was constructed from a backward model, in which the wave number of 1.5 and the body elasticity is tuned to decay to zero and the traveling wave direction is kept towards the tail. The torque was scaled by a factor in each case such that the resultant average amplitude of the motion matched the amplitude at the same viscosity in the experiment. In the forward model, the

elasticity of the body was fixed to $4.5 \times 10^{-12}$ N m$^3$. To stably solve the kinematics (curvature) of the body, we first assumed that at every point of the midline, the curvature was a sinusoidal function of time, i.e., $\kappa(s,t) = A_B(s)\sin[2\pi ft + \phi(s)]$, where the $A_B(s)$ is the amplitude of the curvature, $f$ is the frequency and the value is the same as the input torque, $\phi(s)$ is the phase. We took 11 equally spaced points of $s_i$ and used $A(s_i)$ and $\phi(s_i)$ as the unknown variables for solving the motion. $A_B$ and $\phi$ for any value of $s$ were then linearly interpolated by those corresponding 11 points. Due to the imposed functional form of the curvature, input torque can not be perfectly matched, and the magnitude of the residual torque was ≈5% of the magnitude of the input torque. The resulting phase $\phi(s_i)$ was sometimes non-monotonic near the ends. Therefore, we estimated the spatial frequency by a linear fit of $\phi(s) \approx k_\phi s$, where $0.05 < s < 0.95$ and $k_\phi$ is the fitting parameter. Then the wavelength of the curvature wave was computed as $1/k_\phi$.

## ACKNOWLEDGMENTS

This work was supported by NIH R01AG082039 and NSF Physics of Living Systems Student Research Network (GR10003305).

[1] N. Cohen and J. H. Boyle, Swimming at low Reynolds number: A beginners guide to undulatory locomotion, Contemp. Phys. **51**, 103 (2010).

[2] S. S. Sharpe, Y. Ding, and D. I. Goldman, Environmental interaction influences muscle activation strategy during sand-swimming in the sandfish lizard *Scincus scincus*, J. Exp. Biol. **216**, 260 (2013).

[3] G. V. Lauder and E. D. Tytell, Hydrodynamics of undulatory propulsion, in *Fish Physiology* (Academic Press, New York, 2005), Vol. 23, pp. 425–468.

[4] K. D'Aout, N. A. Curtin, T. L. Williams, and P. Aerts, Mechanical properties of red and white swimming muscles as a function of the position along the body of the eel *Anguilla anguilla*, J. Exp. Biol. **204**, 2221 (2001).

[5] T. McMillen, T. Williams, and P. Holmes, Nonlinear muscles, passive viscoelasticity and body taper conspire to create neuromechanical phase lags in anguilliform swimmers, PLoS Comput. Biol. **4**, e1000157 (2008).

[6] Y. Ding, S. S. Sharpe, K. Wiesenfeld, and D. I. Goldman, Emergence of the advancing neuromechanical phase in a resistive force dominated medium, Proc. Natl. Acad. Sci. USA **110**, 10123 (2013).

[7] B. Jayne and G. Lauder, Red muscle motor patterns during steady swimming in largemouth bass: Effects of speed and correlations with axial kinematics, J. Exp. Biol. **198**, 1575 (1995).

[8] M.-A. Félix and C. Braendle, The natural history of *Caenorhabditis elegans*, Curr. Biol. **20**, R965 (2010).

[9] S. Berri, J. H. Boyle, M. Tassieri, I. A. Hope, and N. Cohen, Forward locomotion of the nematode *C. elegans* is achieved through modulation of a single gait, HFSP Journal **3**, 186 (2009).

[10] C. Fang-Yen, M. Wyart, J. Xie, R. Kawai, T. Kodger, S. Chen, Q. Wen, and A. D. Samuel, Biomechanical analysis of gait adaptation in the nematode *Caenorhabditis elegans*, Proc. Natl. Acad. Sci. USA **107**, 20323 (2010).

[11] X. N. Shen and P. E. Arratia, Undulatory swimming in viscoelastic fluids, Phys. Rev. Lett. **106**, 208101 (2011).

[12] G. Juarez, K. Lu, J. Sznitman, and P. E. Arratia, Motility of small nematodes in wet granular media, Europhys. Lett. **92**, 44002 (2010).

[13] S. Park, H. Hwang, S.-W. Nam, F. Martinez, R. H. Austin, and W. S. Ryu, Enhanced caenorhabditis elegans locomotion in a structured microfluidic environment, PLoS One **3**, e2550 (2008).

[14] T. Majmudar, E. E. Keaveny, J. Zhang, and M. J. Shelley, Experiments and theory of undulatory locomotion in a simple structured medium, J. R. Soc., Interface **9**, 1809 (2012).

[15] T. Wang, C. Pierce, V. Kojouharov, B. Chong, K. Diaz, H. Lu, and D. I. Goldman, Mechanical intelligence simplifies control in terrestrial limbless locomotion, Sci. Robot. **8**, eadi2243 (2023).

[16] J. E. Denham, T. Ranner, and N. Cohen, Signatures of proprioceptive control in *Caenorhabditis elegans* locomotion, Philos. Trans. R. Soc. Lond. B **373**, 20180208 (2018).

[17] V. J. Butler, R. Branicky, E. Yemini, J. F. Liewald, A. Gottschalk, R. A. Kerr, D. B. Chklovskii, and W. R. Schafer, A consistent muscle activation strategy underlies crawling and swimming in *Caenorhabditis elegans*, J. R. Soc., Interface **12**, 20140963 (2015).

[18] D. Porto, Y. Matsunaga, B. Franke, R. M. Williams, H. Qadota, O. Mayans, G. M. Benian, and H. Lu, Conformational changes in twitchin kinase in vivo revealed by FRET imaging of freely moving *C. elegans*, Elife **10**, e66862 (2021).

[19] J. Ding, L. Peng, S. Moon, H. J. Lee, D. S. Patel, and H. Lu, An expanded GCaMP reporter toolkit for functional imaging in *Caenorhabditis elegans*, G3: Genes, Genomes, Genetics **13**, jkad183 (2023).

[20] M. S. Creamer, K. S. Chen, A. M. Leifer, and J. W. Pillow, Correcting motion induced fluorescence artifacts in two-channel neural imaging, PLoS Comput. Biol. **18**, e1010421 (2022).

[21] R. A. Stiernagle, Imaging the activity of neurons and muscles, in *Wormbook*, T. *C. elegans* Research Community (Wormbook, Pasadena, CA, 2006).

[22] See Supplemental Material at http://link.aps.org/supplemental/10.1103/PRXLife.3.023001 for false color videos showing GCaMP (cyan) and RFP (Red) signals of body wall muscles for worms swimming in buffer and crawling on agar.

[23] Q. Wen, M. D. Po, E. Hulme, S. Chen, X. Liu, S. W. Kwok, M. Gershow, A. M. Leifer, V. Butler, C. Fang-Yen, T. Kawano, W. R. Schafer, G. Whitesides, M. Wyart, D. B. Chklovskii, M. Zhen, and A. D. T. Samuel, Proprioceptive coupling within motor neurons drives *C. elegans* forward locomotion, Neuron **76**, 750 (2012).

[24] G. J. Stephens, B. Johnson-Kerner, W. Bialek, and W. S. Ryu, Dimensionality and dynamics in the behavior of *C.* elegans, PLoS Comput. Biol. **4**, e1000028 (2008).

[25] T. Ming and Y. Ding, Transition and formation of the torque pattern of undulatory locomotion in resistive force dominated media, Bioinspir. Biomim. **13**, 046001 (2018).

[26] J. T. Pierce-Shimomura, B. L. Chen, J. J. Mun, R. Ho, R. Sarkis, and S. L. McIntire, Genetic analysis of crawling and swimming locomotory patterns in *C. elegans*, Proc. Natl. Acad. Sci. USA **105**, 20982 (2008).

[27] M. Backholm, W. S. Ryu, and K. Dalnoki-Veress, Viscoelastic properties of the nematode *Caenorhabditis elegans*, a self-similar, shear-thinning worm, Proc. Natl. Acad. Sci. USA **110**, 4528 (2013).

[28] J. Sznitman, X. Shen, R. Sznitman, and P. E. Arratia, Propulsive force measurements and flow behavior of undulatory swimmers at low Reynolds number, Phys. Fluids **22**, 121901 (2010).

[29] J. M. Rieser, B. Chong, C. Gong, H. C. Astley, P. E. Schiebel, K. Diaz, C. J. Pierce, H. Lu, R. L. Hatton, H. Choset, and D. I. Goldman, Geometric phase predicts locomotion performance in undulating living systems across scales, Proc. Natl. Acad. Sci. USA **121**, e2320517121 (2024).

[30] T. Stiernagle, The Maintenance of *C*. elegans, in *Wormbook*, edited by T. *C. elegans* Research Community (Wormbook, 2006).

[31] Y. Cho, D. A. Porto, H. Hwang, L. J. Grundy, W. R. Schafer, and H. Lu, Automated and controlled mechanical stimulation and functional imaging in vivo in *C. elegans*, Lab Chip **17**, 2609 (2017).

[32] J. N. Stirman, M. M. Crane, S. J. Husson, S. Wabnig, C. Schultheis, A. Gottschalk, and H. Lu, Real-time multimodal optical control of neurons and muscles in freely behaving *Caenorhabditis elegans*, Nature Meth. **8**, 153 (2011).

[33] E. Lauga and T. R. Powers, The hydrodynamics of swimming microorganisms, Rep. Prog. Phys. **72**, 096601 (2009).

[34] S.-J. Park, M. B. Goodman, and B. L. Pruitt, Analysis of nematode mechanics by piezoresistive displacement clamp, Proc. Natl. Acad. Sci. **104**, 17376 (2007).